HHS Public Access

Author manuscript

Magn Reson Med. Author manuscript; available in PMC 2014 September 20.

Published in final edited form as:

Magn Reson Med. 2014 March ; 71(3): 934–941. doi:10.1002/mrm.24727.

High Spatial and High Temporal Resolution Dynamic Contrast-Enhanced Perfusion Imaging of the Liver with Time-Resolved 3D-Radial MRI

Ethan K. Brodsky, Ph.D., P.E.[1,2,3], **Eric M. Bultman, B.S.**[1,2], **Kevin M. Johnson, Ph.D.**[2], **Debra E. Horng, BS**[1], **William R. Schelman, MD, Ph.D.**[5], **Walter F. Block, Ph.D.**[2,3], and **Scott B. Reeder, M.D., Ph.D.**[1,2,3,4]

[1]Department of Radiology, University of Wisconsin, Madison, Wisconsin

[2]Department of Medical Physics, University of Wisconsin, Madison, Wisconsin

[3]Department of Biomedical Engineering, University of Wisconsin, Madison, Wisconsin

[4]Department of Medicine, University of Wisconsin, Madison, Wisconsin

[5]Carbone Center Center, University of Wisconsin, Madison, Wisconsin

Abstract

Purpose—Detection, characterization, and monitoring of hepatocellular carcinomas (HCC) in patients with cirrhosis is challenging due to their variable and rapid arterial enhancement. Multiphase dynamic contrast-enhanced MRI (CE-MRI) is used clinically for HCC assessment, but suffers from limited temporal resolution and difficulty in coordinating imaging and breath-hold timing within a narrow temporal window of interest. We demonstrate a volumetric, high spatial resolution, high temporal resolution dynamic contrast enhanced liver imaging method for improved detection and characterization of HCC.

Methods—A time-resolved 3D-radial acquisition with iterative SENSE reconstruction images the entire abdomen and thorax with high spatial and temporal resolution, using real-time 3D fluoroscopy to match the breath-hold to contrast arrival. The sequence was tested on 17 subjects, including 8 patients with HCC or other hyper-vascular focal lesions.

Results—This technique was successful in acquiring volumetric imaging of the entire liver with 2.1 mm isotropic spatial and true 4 s temporal resolution.

Conclusion—This technique may be suitable for detecting, characterizing, and monitoring the treatment of HCC. It also holds significant potential for perfusion modeling, which may provide a non-invasive means to rapidly determine the efficacy of chemotherapeutic agents in these tumors over the entire liver volume.

Keywords

Hepatocellular carcinoma; HCC; liver imaging; perfusion imaging; time-resolved imaging; radial k-space; CE-MRI

Correspondence: Ethan Brodsky, 1125 Wisconsin Institutes for Medical Research, 1111 Highland Avenue, Madison, WI 53705, USA, Phone: 608-265-9687, brodskye@cae.wisc.edu.

Introduction

Hepatocellular carcinoma (HCC) is an enormous health burden, representing the most common primary liver cancer and the third most common cause of cancer mortality worldwide (1). More than 17,000 new cases of liver cancer will be diagnosed in the US this year, and the fatality ratio (mortality/incidence) is approximately one, indicating that the majority of patients with liver cancer do not survive more than a year after diagnosis (2). In addition, the liver is the most common site of metastatic disease from colorectal cancer, which is the third leading cause of cancer in the US (3), and many other common malignancies, including lung cancer, breast cancer, and renal cancer, commonly metastasize to the liver. The ability to accurately diagnose liver tumors, treat these tumors and monitor their response to therapy is of central importance in the treatment of a very large proportion of patients with cancer.

Detection, characterization, and treatment monitoring of HCC in cirrhotic patients is challenging due to their variable and rapid arterial phase enhancement. The liver has a dual blood supply, with normal liver parenchyma perfused primarily (~75%) from portal venous (PV) flow and to a lesser extent (~25%) from hepatic arterial (HA) flow. HCC, however, derives its flow primarily from parasitized hepatic arterial vessels. This behavior can be exploited by dynamic phase contrast enhanced MR imaging to acquire images that capture brisk arterial phase enhancement with subsequent “wash-out”. Multi-phase contrast-enhanced MRI (CE-MRI) is typically used clinically for HCC detection and characterization, but suffers from limited temporal resolution and difficulty in coordinating imaging and breath-hold timing with this narrow temporal window of interest.

Although conventional 3D Cartesian dynamic MRI is commonly used in patients at high risk for HCC, and is considered the most accurate imaging modality for detection and characterization of HCC (4,5), its performance is limited. Specifically, the performance of current MRI methods for detection and characterization of small HCC (< 1–2cm) is relatively poor (6). Further, these methods provide no information on quantitative perfusion. Conventional sequences do not offer adequate spatiotemporal resolution to enable diagnosis of small lesions, with typical resolutions of 1.5–2.0 mm in-plane by 4–8 mm through-plane with a single late arterial phase acquired in a 15–25 s breath-hold (7). The poor through-plane resolution limits detection and characterization of small lesions. The low temporal resolution also limits detection and characterization of lesions due to variations in HCC blood flow and variability in contrast timing and coordination with breath-holding. For patients with known HCC or suspicious lesions, small variations in enhancement resulting from scan-to-scan timing differences can lead to poor repeatability. This leads to inaccurate assessment of tumor changes; resultantly, inconsistent timing between scans can confound assessments of disease progression or treatment effectiveness. Pandharipande *et al.* suggests that volumetric imaging with spatial resolution of 2 mm in each dimension and temporal resolution of 3 s or better is desirable (8). One approach that has been used to avoid mis-timing is the use of three 5–10s breath-holds during the arterial phase, with the goal of obtaining at least one frame with adequate enhancement (7). Although effective, this approach requires significant trade-offs in spatial resolution and also does not provide

quantitative information on tumor perfusion. There is an unmet need for acquisition strategies that can simultaneously provide both good spatial and temporal resolution. A variety of novel approaches have been proposed (9,10,11,12), but none have gained clinical acceptance.

In recent years, anti-angiogenic agents such as sorafenib and bevacizumab (13) have been shown to prolong survival in patients with advanced HCC and colorectal metastases, respectively. Currently, monitoring tumor response requires long periods (months) of chemotherapy to identify changes in tumor size in accordance with RECIST criteria (14). Importantly, some tumors that respond to these agents are stabilized, but may not demonstrate changes in size. Anti-angiogenic agents are well known to disrupt the microvasculature of tumors very rapidly, within just hours or a few days, with tumor size subsequently stabilizing or decreasing over a course of many weeks or months (13,15). Early detection of changes in tumor vascularity offers a unique opportunity to rapidly determine whether an agent is effective against the tumor. Detecting early biomarkers of tumor therapy response would have a profound impact on clinical treatment decisions for treatment of liver tumors, with the potential for significant impact on effectiveness and cost of therapy.

The purpose of this work is to demonstrate the implementation and feasibility of a volumetric, high spatial resolution, high temporal resolution dynamic contrast enhanced liver imaging method for improved detection and characterization of HCC. Such a sequence would also hold potential for quantitative perfusion imaging to provide a non-invasive means of rapidly determining the efficacy of chemotherapeutic agents in liver tumors over the entire liver. This would offer the potential to save patients from lengthy periods of treatment with ineffective and expensive agents that have toxic side effects by more rapidly determining the best agent for a patient’s particular tumor.

Materials and Methods

Acquisition Sequence

The acquisition sequence is an extension of a time-resolved undersampled multi-echo 3D radial spoiled gradient-recalled echo (VIPRME-SPGR) acquisition sequence (16,17) with real-time 3D fluoroscopy (18).

The scan samples k-space uniformly using half-echoes sampling radial lines during interleaved subframes acquired at 1 s intervals, with bit-reversal (19) over all subframes collected in the entire exam as a basis for the interleaving. As shown in Figure 1, four half-echoes are collected on four different radial lines after each excitation, using short tangential blips at the edge of k-space and a bend at the center of k-space to move between projection angles. Ramp sampling is used to improve sampling efficiency.

Patients were scanned on a clinical GE Healthcare 3.0 T MR750 scanner (GE Healthcare; Waukesha, WI) using a 32-channel phased array torso receiver coil (Necoil; Pewaukee, WI) that provided coverage over the entire abdomen and also the lower thorax, useful for visualization of contrast arrival and fluoro-triggering.

Seventeen subjects were scanned after IRB approval and informed consent, including eight patients with known or suspected HCC. The sequence imaged a 48 cm spherical FOV (limited by a 32–40 cm axial slab excitation) with an effective readout length of 224 evenly spaced points, for an isotropic spatial resolution of 2.1 mm, in a total scan time of 180 s (62,280 excitations). The TR was 2.9 ms, TEs were 0.4/1.0/1.7 ms, and receiver bandwidth was±250 kHz, with a flip angle of 12°. A flip angle of 12° was chosen to achieve the best balance of SNR performance and linearity of signal with gadolinium concentration, using methods developed for quantitative renal perfusion imaging (20). The acquisition was interleaved such that k-space was sampled uniformly using 346 excitations sampling 1384 half-echoes on unique radial lines during each 1 s subframe, with each subframe undersampling k-space by a factor of 114. The pulse sequence control program also recorded position of the respiratory bellows at every tenth acquisition.

One subject with Focal Nodular Hyperplasia (FNH) was scanned using an earlier version of this acquisition on a GE HealthCare 1.5T Signa HDx TwinSpeed magnet and an eight-channel body array coil. The acquisition was identical except that FOV was 40 cm, effective readout length was 256 samples for an acquired isotropic resolution of 1.6 mm (reconstructed at the same 2.1 mm used for the later scans), total scan time was 120 s (26,160 excitations), with a TR of 4.6 ms, TEs of 0.3/1.7/3.1 ms, receiver bandwidth of ±125 kHz, and a flip angle of 25°.

At the end of each exam, a low-resolution conventional 3D Cartesian SPGR sequence was acquired twice, once with the same coil used for the time-resolved sequence, and once with the body coil. These datasets were used to generate coil sensitivity maps for post-processing with perfusion modeling algorithms.

All image datasets were reviewed by a board-certified radiologist with 12 years of experience in abdominal MRI.

Monitoring with real-time 3D fluoroscopy

To aid in proper timing of the breath-hold interval, each subject was monitored throughout the scan using real-time 3D fluoroscopy (18). The real-time system displayed axial, coronal, and sagittal limited maximum intensity projections (MIPs) of a low-resolution 3D volume image with 5 mm isotropic resolution at a rate of one frame per second, with each frame based on the preceding two seconds of collected data, using the exact same data acquired for the high-resolution scan, but reconstructed at a much lower spatial resolution.

Experimental Protocol

Each subject was instructed to conduct four separate breath-holds on expiration during the course of the scan, with verbal coaching using headphones and the scanner’s voice communication system. The first breath-hold was begun at the start of the scan and lasted approximately ten seconds. Ten to fifteen seconds into the scan, 0.1 mmol/kg gadobenate dimeglumine (MultiHance, Bracco Diagnostics; Princeton, NJ) was injected at 3 ml/s, followed by a 25 ml saline flush at 2–3 ml/s. When the real-time 3D fluoroscopy showed contrast arrival in the heart (typically 20–40 s into the scan), the subject was coached to perform a 20–30 s breath-hold, targeted to cover the period of early and late hepatic arterial

enhancement in the liver. After a few breaths, the patient was coached to perform a second 20–30 s breath-hold, targeted to cover the portal venous phase (typically 50–80 s after injection). Finally, the patient performed a third 20–30 s breath-hold near the end of the scan, to capture a delayed phase of liver enhancement. Data collection occurs continuously throughout the scan, during both periods of breath-hold and free-breathing.

Image Reconstruction

3D volume images were reconstructed at 1 s intervals using data from a 4 s sliding window, for an effective undersampling factor of 29 and a true temporal footprint of 4 s (21). To yield acceptable image quality with the high undersampling associated with such a narrow temporal aperture, reconstruction was based on an auto-calibrated iterative non-Cartesian sensitivity-encoding (SENSE) algorithm (22) with data consistency weighting constraints, which reconstructs images according to the following equation:

$$x=\arg\min_{x}\left\{\|G^{1/2}(Ex-s)\|_2^2+\lambda\|imag(x)\|_2^2\right\} \quad \text{Equation 1}$$

where G is a data weighting term, E is the encoding matrix which transforms images to k-space including Fourier and coil sensitivity terms, x is the output image, s is the raw data, λ is a regularization parameter, and *imag( )* is a function that returns the imaginary component of an image. The left term of Equation 1 represents a data consistency term while the right term enforces Hermitian symmetry on the assumption that most of the phase is subtracted out by the coil sensitivity estimates (25). Coil sensitivity maps are estimated from the fully sampled, central k-space data of all projections from the center echo time (23). These projections have substantial respiratory motion; but motion artifacts are negligible due to the diffuse sampling pattern, low resolution, and nearly in-phase TE.

To prevent errors due to inconsistent signals between the three echo times, we utilize a weighted least squares technique that treats data inconsistency as an additional noise source (24). This technique utilizes estimates of signal evolution to approximate point-by-point errors in the signal in references to some desired image contrast. These inconsistencies can be caused by phase differences between echoes from off-resonant signal (due to fat or B_0 inhomogeneity), magnitude differences due to T_2* decay, or slight patient motion between excitations. In this work, we approximate signal evolution as weighted combination of fat and water with a Gaussian distributions for fat and water, each with full width half maximum (FWHM) of 100 Hz, a modeled water:fat ratio of 2:1 and average $T2^*$ of 50 ms. The data consistency error is subsequently determined as the signal difference from the central echo time and the weight G is selected to be the inverse of the expected error. As shown in previous work (24) this effectively deemphasizes the early and late echoes over the center echo.

Equation 1 was minimized using conjugate gradient least squares with optimized gridding routines (26). The final images were reconstructed with 2.1 mm isotropic resolution interpolated onto a 1.6 mm (256×256×256) grid at 1 s intervals using a 4 s rectangular sliding window.

Breath-hold period detection

Periods of consistent breath-holding were identified by visual inspection of graphs of the waveforms recorded by the respiratory bellows and recorded with their endpoints quantized to the nearest 1 s. Breath-hold periods were also estimated using the DC signal from each view by using the first sample from each readout. After complex summation to combine data from all receiver coils (27) and temporal low-pass filtering with a hard 4 Hz cutoff, the magnitude and phase of this value was plotted against time and the breath-hold intervals identified by visual inspection (28).

Semi-quantitative Perfusion Modeling

A full treatment of perfusion modeling is outside the scope of this work, but we show here some initial work in semi-quantitative perfusion modeling from these datasets. To prepare image data for perfusion modeling, reconstructed image volumes (3D Cartesian) were weighted using a coil sensitivity map generated with the two low-resolution conventionally-acquired datasets (29). To further mitigate the effect of non-uniform B_1 surface coil sensitivity, the signal value at each voxel for each timeframe was recast as a ratio of its signal at that timeframe to its peak signal during the 180s scan.

The time-resolved image datasets were subsequently post-processed using semi-quantitative perfusion monitoring algorithms (30). Time to arrival (TTA) maps were generated by examining the signal intensity at each voxel in each timeframe and selecting the first timeframe during a breath-hold period in which the signal of that voxel reached 85% of its peak level over the entire time course. TTA values were normalized to the arrival time for a 1 cm segmented slab in the aorta, which was defined as the reference time for contrast arrival (0 s).

Area under curve (AUC) maps were generated by summing the signal at each voxel across timeframes corresponding to the arterial-phase breath-hold. Arterial-phase images were used when determining this parameter so that the rapid enhancement of hypervascular lesions compared to the rest of the liver would be reflected in the final parameter maps. The AUC value at each voxel was divided by the mean AUC of a 1 cm segmented slab of aorta in order to normalize the final AUC parameters to the contrast input.

Results

For all exams, patient monitoring using real-time 3D fluoroscopy was successful in detecting contrast arrival in the heart, which facilitated subject coaching to match the arterial-phase breath-hold with contrast arrival in the liver. The 3D fluoroscopy system displayed a set of three orthogonal MIP images at 1 s intervals, each based on the preceding two seconds of data. Latency between completion of the acquisition of each sub-frame and the subsequent reconstruction is approximately 250 ms (18). A subset of the fluoroscopic images from one exam showing contrast arrival in the right heart, left heart, aorta, and other major organs is shown in Figure 2.

The radiologist who reviewed the datasets found image quality to be good to excellent in all subjects. Representative images from a number of patient scans demonstrate the ability of

this technique to consistently capture the enhancement dynamics of focal liver lesions. Figure 3 shows axial image slices with 4 s temporal aperture acquired during the arterial, portal venous and delayed phases of enhancement in a patient with a large FNH lesion. The arterial-phase enhancement of the FNH is clearly captured during the first breath hold, while two subsequent breath-holds show that the lesion has become isointense with surrounding hepatic parenchyma. Figure 4 shows 4 mm thick arterial-phase axial and coronal image reformats, also with 4 s temporal aperture, from a patient with numerous HCC lesions distributed throughout the liver. Multiple HCCs, including several sub-centimeter lesions, are visualized in Figure 4(a). The coronal slice in Figure 4(b) demonstrates the large volumetric coverage afforded by the 3D radial acquisition, in addition to the effect of the narrow temporal footprint: the selected frame shows significant hepatic arterial enhancement without portal venous contamination. Figure 5 shows coronal thin-slab (5.6 cm) MIPs from the arterial-phase breath hold in a healthy volunteer. In Figure 5(a), the common hepatic artery and its branches, as well as the renal arteries and splenic artery, are all clearly depicted; Figure 5(b), also acquired during the first breath hold, depicts the portal vein and its intrahepatic branches as well as the renal veins and splenic vein.

Figure 6 shows axial slices and coronal reformats from a 64 year old female patient undergoing Sorafenib therapy to treat HCC. Images from the arterial, portal venous, and delayed phase show rapid initial uptake of contrast into the lesions during the arterial phase, washout during the portal venous phase, and equilibration with surrounding tissue during the delayed phase.

Perfusion modeling

This acquisition generates 180 volume datasets with 256×256×256 matrix reconstructed at 1 s intervals (120 frames for the 1.5 T dataset), each based on a 4 s sliding-window of data. Due to the low flip angle, signal intensity is approximately proportional to contrast concentration in the voxel (20), making these datasets amenable to post-processing and analysis with both quantitative and non-quantitative modeling algorithms. Figure 7 shows images from perfusion modeling for a patient with numerous HCC lesions. The lesions are clearly visible in the time-to-arrival (TTA) and area-under-curve (AUC) maps. While the lesions can also be seen in the arterial phase image, these automatically generated images may simplify rapid assessment by eliminating the need to first identify an arterial frame.

Figure 7(a) shows an average arterial-phase image slice so that all enhancing HCCs can be visualized. Figure 7(b) shows a time-to-arrival map overlaid on the arterial phase slice. Voxels within most HCC lesions demonstrate significantly shorter TTA values than surrounding hepatic parenchyma; this is consistent with the hepatic arterial blood supply of HCCs. Figure 7(c) shows an arterial-phase AUC map overlaid on the image slice. Most of the lesions that demonstrate rapid arrival time on the TTA map have significantly greater AUC than the surrounding normal liver tissue. The arrival time map aids in distinguishing early-enhancing (true) lesions from other later-enhancing features that might be seen in a slightly mistimed arterial frame (e.g. the section of portal vein marked with arrows).

Breath-hold Period Identification

While data from the respiratory bellows were used in this study to identify the period of stable subject breath-hold, the correspondence between this curve and the DC contrast waveforms, as shown in Figure 8, suggests that periods of respiratory stability could be reliably identified without using respiratory bellows (28).

Discussion

In this work we have demonstrated the feasibility of obtaining high spatial and temporal resolution images of the liver using a time-resolved 3DPR sequence with an iterative constrained reconstruction. Using this method, we have been able to achieve isotropic 2.1 mm spatial resolution over a 48 cm FOV with true 4 s temporal resolution. With real-time imaging and a time-resolved scan with coverage of the entire abdomen and thorax, it was possible to consistently match breath-holds with contrast arrival, guaranteeing good depiction of the hepatic arterial and portal venous phases of enhancement.

Time-resolved 3DPR sequences offer substantial advantages in flexibility in that the same data can be reconstructed in a variety of different ways, making tradeoffs between spatial resolution, temporal resolution, and image quality after acquisition. This enables 3D fluoroscopy to occur simultaneously with high-resolution 3D imaging using a single sequence. The multi-echo pulse sequence offers very high acquisition efficiency, with data being collected during 47% of each readout. With the consistency-weighted reconstruction algorithm, data acquired at varying echo times is combined effectively, even in the presence of phase inconsistencies due to T2*, off-resonant spin in areas of B_0 inhomogeneity, or inconsistencies from respiratory motion. The isotropic resolution is beneficial because it allows for image reformatting into a variety of orientations. In clinical use, perfusion modeling artifacts associated with inconsistencies between successive breath-holds can be dealt with using rigid-body motion correction, a topic explored by Bultman *et al* (31).

The major limitations of this work stem from the non-Cartesian nature of the acquisition and the computationally intensive iterative processing required for image reconstruction. The current C-based implementation of the reconstruction takes 14 minutes per frame (42 hours total for 180 frames) on a computer with four AMD Opteron 6136 2.4 GHz processors (each with eight cores) and 80 GB of memory. However, with further optimization it could easily be made orders of magnitude faster. Reconstructing volume images with a 4 s temporal frame rate (the 1 s temporal resolution used here is clinically unnecessary) would lead to a 4× speedup, and reconstructing images only during breath-holding periods would reduce reconstruction time by an additional factor of 2–3×. The reconstruction process is also trivially parallelizable on a per-frame basis, so it could be distributed over multiple computers for a speedup proportional to the number of machines. Future use and implementation of this method will employ additional optimization to improve image reconstruction times to clinically acceptable levels.

Several emerging view sharing methods may offer similar performance. Differential Subsampling with Cartesian Ordering (9) uses pseudo-random variable-density sampling on a Cartesian grid with multiple echo times to provide fat/water separation. Published results

show that DISCO offers somewhat higher in-plane spatial resolution (1.1 mm × 1.5 mm) but poorer through-plane resolution (3.0 mm) compared to the 2.1 mm isotropic resolution of our technique. Although this method cites a temporal resolution of 4 s, due to view-sharing of interleaved outer regions of k-space, the temporal footprint is 15.6 s, so depiction of rapid temporal dynamics may be compromised compared to the true 4 s resolution with our technique. HighlY constrained Cartesian Reconstruction (10) is similar pseudo-Cartesian approach that combines pseudo-random variable density sampling on the k_y–k_z plane matrix with a multiplicative constrained parallel image reconstruction. Reported spatial resolution is higher than that of our technique (0.94 × 0.94 × 1.8 mm^3 vs. 2.1 mm isotropic), although temporal resolution is worse (~8 s vs. 4 s) and coverage is smaller. Temporal Resolution Acceleration with Constrained Evolution Reconstruction (12) uses a stack of variable density spirals with golden ratio view ordering and constrained evolution reconstruction to give better in-plane resolution than our technique (1.3 mm) but worse through-plane (5 mm). The temporal fidelity varies with spatial frequency and is based on the assumption that temporal changes are small at short time intervals. Finally, the volume of coverage using these three methods (DISCO, HYCR and TRACER), although adequate for most cases, is much smaller than that using the 3DPR approach. For assessing the effectiveness of new therapeutic agents, a short simple temporal window may be preferable to compressed sensing approaches that depend on assumptions as to temporal dynamics.

Conclusion

We have presented a method for volumetric imaging of the entire liver with 2.1 mm isotropic spatial and true 4 s temporal resolution. This technique may be suitable for detecting, characterizing, and monitoring the treatment of HCC. It also holds significant potential for quantitative perfusion imaging, which may provide a non-invasive means to rapidly determine the efficacy of chemotherapeutic agents in these tumors over the entire liver volume.

Acknowledgments

This work was supported by the NIH (RC1 EB010384, R01 DK083380, R01 DK088925, R01 DK096169), an RSNA Research Scholar Grant, a University of Wisconsin System Applied Research Grant, and GE Healthcare.

References

1. Jackson A, Haroon H, Zhu XP, Li KL, Thacker NA, Jayson G. Breath-hold perfusion and permeability mapping of hepatic malignancies using magnetic resonance imaging and a first-pass leakage profile model. NMR Biomed. 2002; 15(2):164–173. [PubMed: 11870912]
2. Abdullah SS, Pialat JB, Wiart M, Duboeuf F, Mabrut JY, Bancel B, Rode A, Ducerf C, Baulieux J, Berthezène Y. Characterization of hepatocellular carcinoma and colorectal liver metastasis by means of perfusion MRI. J Magn Reson Imaging. 2008; 28(2):390–395. [PubMed: 18666145]
3. Hagiwara M, Rusinek H, Lee VS, Losada M, Bannan MA, Krinsky GA, Taouli B. Advanced liver fibrosis: diagnosis with 3D whole-liver perfusion MR imaging--initial experience. Radiology. 2008; 246(3):926–934. [PubMed: 18195377]
4. Sersté T, Barrau V, Ozenne V, Vullierme MP, Bedossa P, Farges O, Valla DC, Vilgrain V, Paradis V, Degos F. Accuracy and disagreement of computed tomography and magnetic resonance imaging for the diagnosis of small hepatocellular carcinoma and dysplastic nodules: role of biopsy. Hepatology. 2012; 55(3):800–806. [PubMed: 22006503]

5. Becker-Weidman DJ, Kalb B, Sharma P, Kitajima HD, Lurie CR, Chen Z, Spivey JR, Knechtle SJ, Hanish SI, Adsay NV, Farris AB 3rd, Martin DR. Hepatocellular carcinoma lesion characterization: single-institution clinical performance review of multiphase gadolinium-enhanced MR imaging--comparison to prior same-center results after MR systems improvements. Radiology. 2011; 261(3): 824–833. [PubMed: 21969663]
6. Forner A, Vilana R, Ayuso C, Bianchi L, Solé M, Ayuso JR, Boix L, Sala M, Varela M, Llovet JM, Brú C, Bruix J. Diagnosis of hepatic nodules 20 mm or smaller in cirrhosis: Prospective validation of the noninvasive diagnostic criteria for hepatocellular carcinoma. Hepatology. 2008; 47(1):97–104. [PubMed: 18069697]
7. Merkle EM, Szklaruk J, Taouli B. Imaging techniques in the diagnosis of hepatocellular carcinoma and metastatic carcinoma as a result of colon cancer. Gastroenterol Hepatol (NY). 2010; 6(8):1–16.
8. Pandharipande PV, Krinsky GA, Rusinek H, Lee VS. Perfusion Imaging of the Liver: Current Challenges and Future Goals. Radiology. 2005; 234(3):661–673. [PubMed: 15734925]
9. Saranathan M, Rettmann DW, Hargreaves BA, Clarke SE, Vasanawala SS. DIfferential Subsampling with Cartesian Ordering (DISCO): a high spatio-temporal resolution Dixon imaging sequence for multiphasic contrast enhanced abdominal imaging. J Magn Reson Imag. 2012; 35(6): 1484–1492.
10. Wang K, Busse RF, Holmes JH, Beatty PJ, Brittain JH, François CJ, Reeder SB, Du J, Korosec FR. Interleaved variable density sampling with a constrained parallel imaging reconstruction for dynamic contrast-enhanced MR angiography. Magn Reson Med. 2011; 66(2):428–436. [PubMed: 21360740]
11. Song HK, Dougherty L. Dynamic MRI with projection reconstruction and KWIC processing for simultaneous high spatial and temporal resolution. Magn Reson Med. 2004; 52(4):815–824. [PubMed: 15389936]
12. Xu B, Spincemaille P, Chen G, Agrawal M, Nguyen TD, Prince MR, Wang Y. Fast 3D contrast enhanced MRI of the liver using temporal resolution acceleration with constrained evolution reconstruction. Magn Reson Med. 2012 In Press. EarlyView. 10.1002/mrm.24253
13. Bosch FX, Ribes J, Borras J. Epidemiology of primary liver cancer. Semin Liver Dis. 1999; 19(3): 271–285. [PubMed: 10518307]
14. Eisenhauer EA, Therasse P, Bogaerts J, Schwartz LH, Sargent D, Ford R, Dancey J, Arbuck S, Gwyther S, Mooney M, Rubinstein L, Shankar L, Dodd L, Kaplan R, Lacombe D, Verweij J. New response evaluation criteria in solid tumours: revised RECIST guideline (version 1. 1). Eur J Cancer. 2009; 45(2):228–247. [PubMed: 19097774]
15. Jemal A, Siegel R, Ward E, Hao Y, Xu J, Murray T, Thun MJ. Cancer statistics, 2008. CA Cancer J Clin. 2008; 58(2):71–96. [PubMed: 18287387]
16. Barger AV, Block WF, Toropov Y, Grist TM, Mistretta CA. Time-resolved contrast enhanced imaging with isotropic resolution and broad coverage using an undersampled 3D projection trajectory. Magn Reson Med. 2002; 48(2):297–305. [PubMed: 12210938]
17. Brodsky, E.; Lu, A.; Thornton, FJ.; Grist, TM.; Block, WF. Using Multiple Half-Echos to Improve Sampling Efficiency and Fat Suppression in Time-Resolved MRA. Proceedings of the 11th Annual Meeting of ISMRM; Toronto, Ontario, Canada. 2003. p. 322
18. Brodsky E, Isaacs D, Grist TM, Block WF. 3D Fluoroscopy with real-time 3D non-Cartesian phased-array contrast-enhanced MRA. Magn Reson Med. 2006; 56(2):247–254. [PubMed: 16791862]
19. Sedarat H, Kerr AB, Pauly JM, Nishimura DG. Partial-FOV Reconstruction in Dynamic Spiral Imaging. Magn Reson Med. 2000; 43(3):429–439. [PubMed: 10725886]
20. Bokacheva L, Rusinek H, Chen Q, Oesingmann N, Prince C, Kaur M, Kramer E, Lee VS. Quantitative determination of Gd-DTPA concentration in T1-weighted renography studies. Magn Reson Med. 2007; 57(6):1012–1018. [PubMed: 17534906]
21. Haider CR, Hu HH, Campeau NG, Huston J 3rd, Riederer SJ. 3D high temporal and spatial resolution contrast-enhanced MR angiography of the whole brain. Magn Reson Med. 2008; 60(3): 749–760. [PubMed: 18727101]
22. Pruessmann KP, Weiger M, Bornert P, Boesiger P. Advances in sensitivity encoding with arbitrary k-space trajectories. Magn Reson Med. 2001; 46(4):638–651. [PubMed: 11590639]

23. McKenzie CA, Yeh EN, Ohliger MA, Price MD, Sodickson DK. Self-calibrating parallel imaging with automatic coil sensitivity extraction. Magn Reson Med. 2002; 47(3):529–538. [PubMed: 11870840]

24. Johnson KM, Block WF, Reeder SB, Samsonov A. Improved least squares MR image reconstruction using estimates of k-space data consistency. Magn Reson Med. 2012; 67(6):1600–1608. [PubMed: 22135155]

25. Bydder M, Robson MD. Partial Fourier Partially Parallel Imaging. Magn Reson Med. 2005; 53:1393–1401. [PubMed: 15906299]

26. Beatty PJ, Nishimura DG, Pauly JM. Rapid Gridding Reconstruction With a Minimal Oversampling Ratio. IEEE Trans Med Imaging. 2005; 24(6):799–808. [PubMed: 15959939]

27. Roemer PB, Edelstein WA, Hayes CE, Souza SP, Mueller OM. The NMR Phased Array. Magn Reson Med. 1990; 16(2):192–225. [PubMed: 2266841]

28. Horng, DE.; Brodsky, EK.; Reeder, SB. Validation of DC Self-Navigation for Breath-hold Period Identification in Contrast-Enhanced 3D Radial Liver Perfusion Imaging. Proceedings of the Nineteenth Annual Meeting of ISMRM; Montreal, Quebec, Canada. 2011. p. 2673

29. Narayana PA, Brey WW, Kulkarni MV, Sievenpiper CL. Compensation for surface coil sensitivity variation in magnetic resonance imaging. Magn Reson Imag. 1988; 6(3):271–4.

30. Collins DJ, Padhani AR. Dynamic magnetic resonance imaging of tumor perfusion. IEEE Eng Med Biol Mag. 2004; 23(5):65–83. [PubMed: 15565801]

31. Bultman, E.; Horng, D.; Brodsky, EK.; Johnson, KM.; Reeder, SB. Simple Motion Correction for Hepatic DCE-MRI: Registration of Sequential Breath Holds in 3D Radial Time-Resolved Scans. Proceedings of the 20th Annual Meeting of ISMRM; Melbourne, Australia. 2012. p. 1965

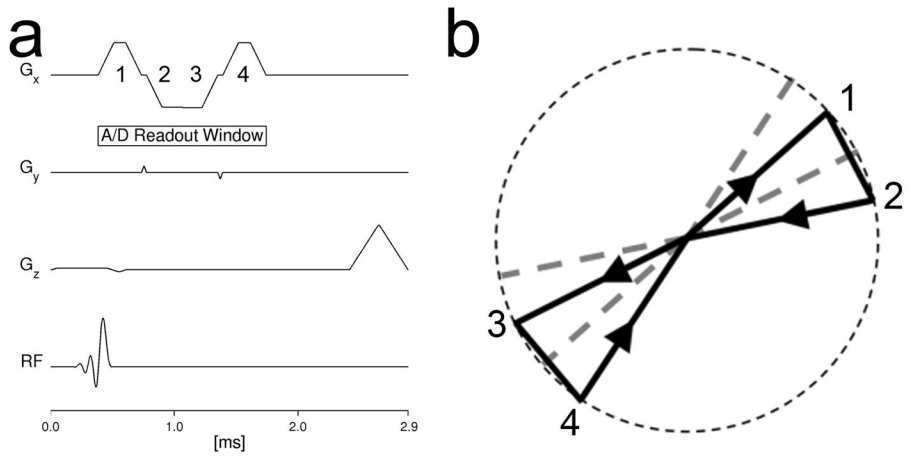

Figure 1.

Pulse sequence (a) and k-space trajectory (b) for the multi-echo 3D radial acquisition used in this work. Following an axial thick slab excitation, four half-echoes are collected at four unique radial projection angles, sampling a sphere in k-space.

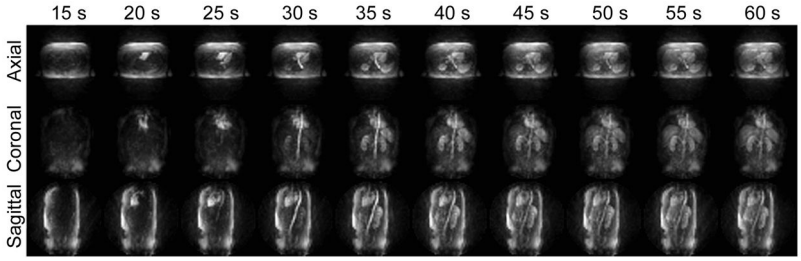

Figure 2.

3D fluoroscopic images displayed in real-time during the scan show initial contrast arrival in the heart in time to allow the subjected to be coached into a breath-hold before the beginning of arterial enhancement. Limited MIPs (24 cm thick for axial and sagittal, 10 cm thick for coronal) show an overview of the entire thoracic and abdominal vascular system.

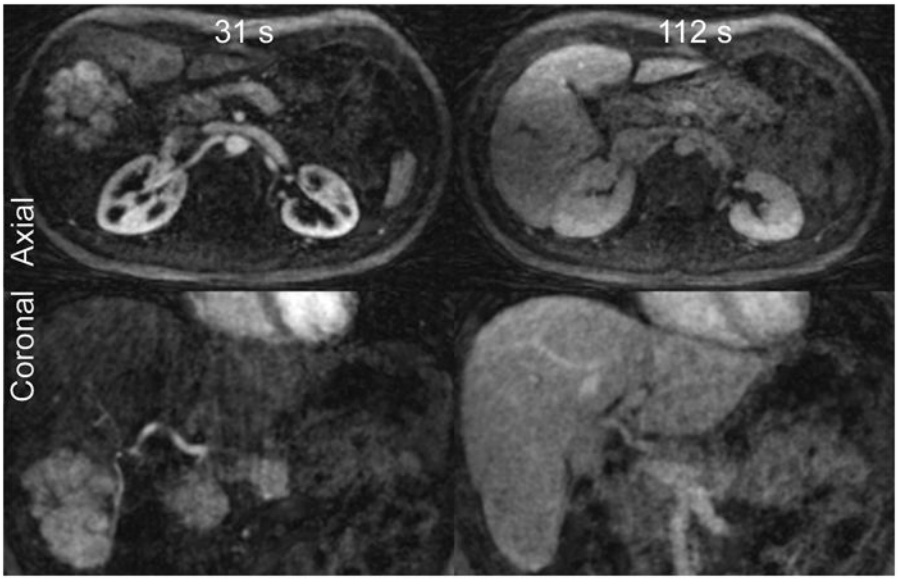

Figure 3.

Axial and coronal images (2 mm slices) from a 1.5T exam of a patient with a large FNH lesion in the liver. While arterial-phase images at 31 s post-injection show significant contrast uptake by the FNH lesion, the lesion has become isointense with the surrounding normal liver in early delayed-phase images at 112 s.

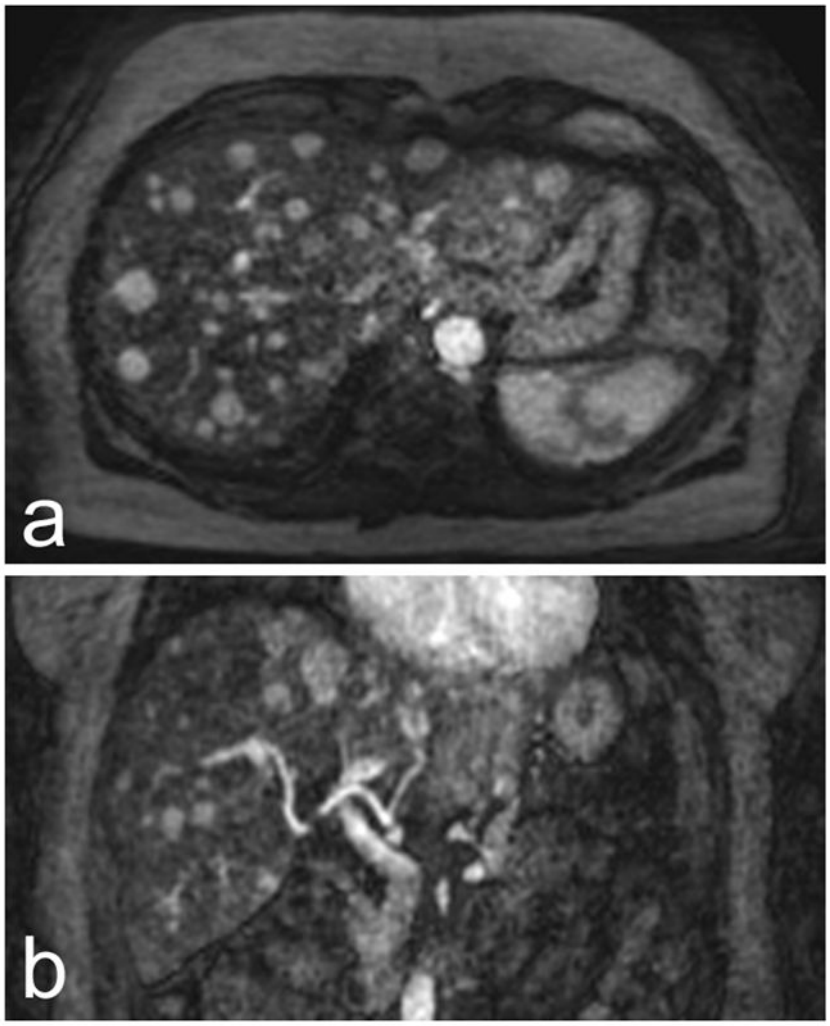

Figure 4.

Axial (a) and coronal (b) coil sensitivity-corrected 4 mm arterial-phase image reformats from a 3T exam of a patient with multiple HCCs. Numerous focal lesions, including several smaller than 1 cm, can be seen in (a). (b) Demonstrates the full-liver volumetric coverage afforded by the VIPRME acquisition. Also note that complete enhancement can be seen in the hepatic artery while portal vein enhancement is minimal, demonstrating the benefit of continuous acquisition with retrospective timeframe identification.

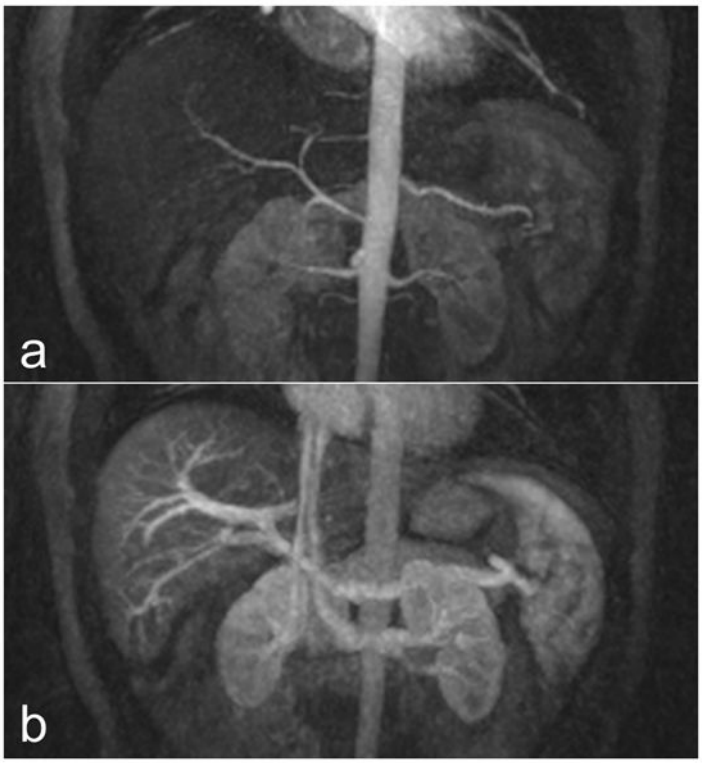

Figure 5.

Images from a 3T exam of a healthy volunteer demonstrate the angiographic performance of the VIPRME acquisition. (a) Shows an arterial-phase 5.6 cm thin-slab coronal MIP, which depicts the splenic and renal arteries in addition to the hepatic artery and its branches. (b) Shows a 5.6 cm thin-slab coronal MIP acquired during the arterial phase breath hold which depicts the portal vein and branches, renal vein and splenic vein. Note that this MIP corresponds to a timeframe only 10 s later than that in (a).

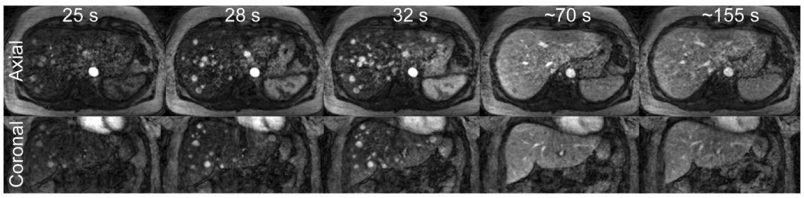

Figure 6.

Axial (top row) and coronal (bottom row) slices during the arterial phase (25 s, 28 s, 32 s post-injection), portal venous phase (~70 s), and delayed phase (~155 s) show early enhancement and later washout of contrast in lesions in a patient with HCC.

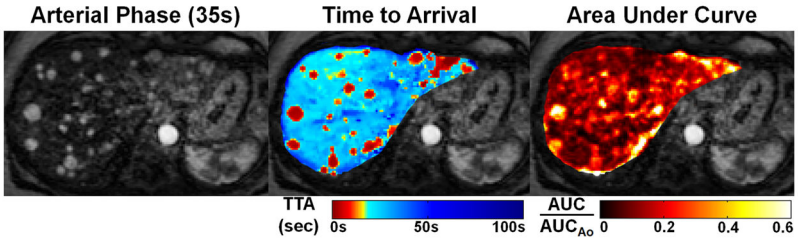

Figure 7.

The time-resolved linear-contrast volume datasets are suitable to for use as source data for quantitative perfusion modeling. (a) Shows a single-slice axial image of a patient with numerous HCCs averaged over the 20 s arterial phase breath hold. (b) and (c) Show time-to-arrival (TTA) and area under the curve (AUC) parameter maps overlaid on this slice. As seen on the TTA map, the HCC lesions demonstrate arrival times consistent with arterial as opposed to portal venous perfusion. The AUC map depicts several large lesions with greater summed arterial phase signal than normal hepatic parenchyma.

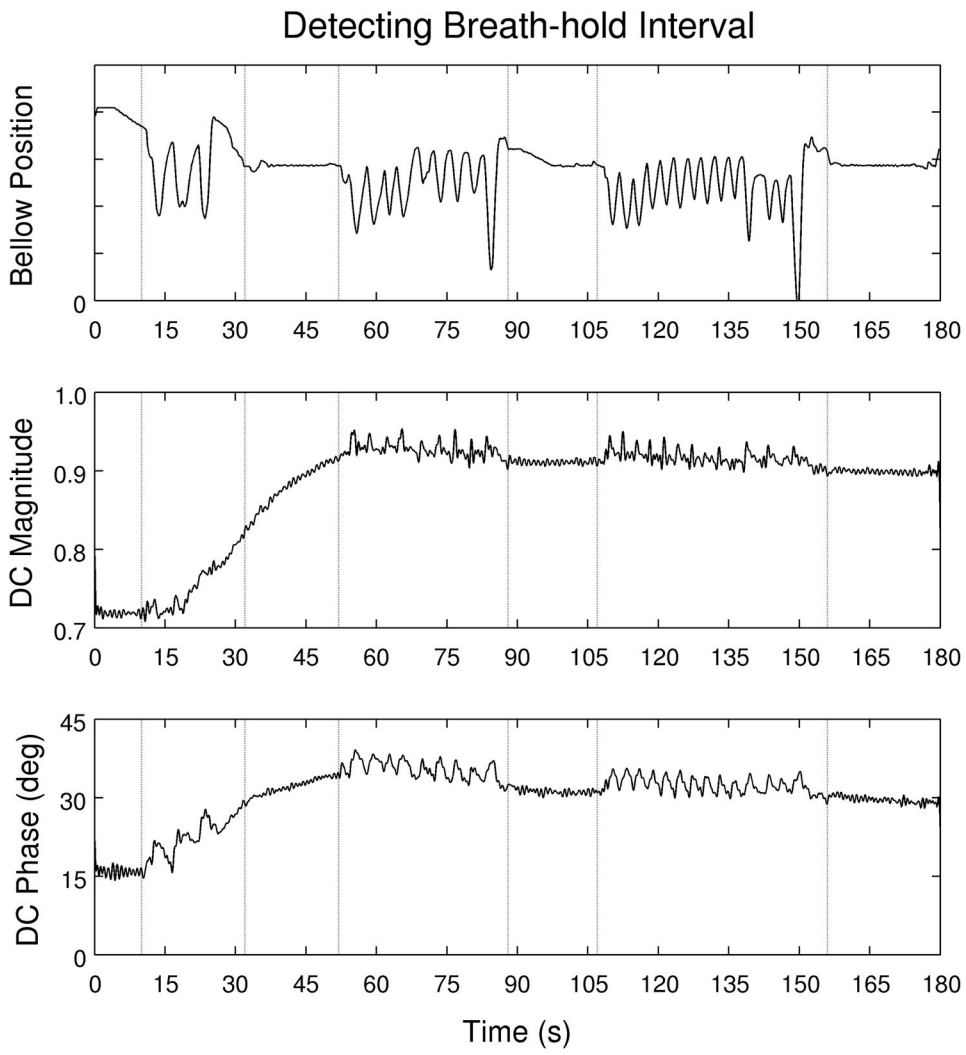

Figure 8.

The subject was coached through four periods of breath holding during the scan. Respiratory waveforms collected using bellows shows the endpoints of each of these intervals and allows assessment of how consistently the subject actually maintained the breath-hold. Plots of the magnitude and phase of DC signal from the first sample of each readout suggests that breath-hold intervals could also be detected from this data directly, should respiratory bellow data not be available.